Coating gold nanorods with silica prevents the generation of reactive oxygen species under laser light irradiation for safe biomedical applications

Sarra Mitiche, Syrine Gueffrache, Sylvie Marguet, Jean-Frédéric Audibert, Robert Bernard Pansu, Bruno Palpant

ARTICLE

Coating gold nanorods with silica prevents the generation of reactive oxygen species under laser light irradiation for safe biomedical applications

Received 00th January 20xx,
Accepted 00th January 20xx

DOI: 10.1039/x0xx00000x

Sarra Mitiche[a], Syrine Gueffrache[a], Sylvie Marguet[b], Jean-Frédéric Audibert[c], Robert Bernard Pansu[a], Bruno Palpant[a*]

Gold nanoparticles can produce reactive oxygen species (ROS) under the action of ultrashort pulsed light. While beneficial for photodynamic therapy, this phenomenon is prohibitive for other biomedical applications such as imaging, photo-thermal drug release, or targeted gene delivery. Here, ROS are produced in water by irradiating gold nanorods and silica-coated gold nanorods with near-infrared femtosecond laser pulses and are detected using two fluorescent probes. Our results demonstrate that a dense silica shell around gold nanorods inhibits the formation of singlet oxygen ($^1O_2$) and hydroxyl radical ($OH^•$) efficiently. The silica coating prevents the Dexter energy transfer between the nanoparticles and $^3O_2$, stopping thus the generation of $^1O_2$. In addition, numerical simulations accounting for the use of ultrashort laser pulses show that the plasmonic field enhancement at the nanoparticle vicinity is lessened once adding the silica layer. With the multiphotonic ejection of electrons being also blocked, all the possible pathways for ROS production are hindered by adding the silica shell around gold nanorods, making them safer for a range of biomedical developments.

Introduction

Reactive oxygen species (ROS) are highly reactive and cytotoxic chemical molecules.[1,2] They include singlet oxygen ($^1O_2$), superoxide anion (O_2^-), hydroxyl radical (•OH), and hydrogen peroxide (H_2O_2). When exploited in the Photo-Dynamic Therapy (PDT), ROS are generally produced from the interaction of light and photosensitizing molecules. However, recent works have shown that it is possible to generate ROS efficiently from the interaction of noble metal nanoparticles and light, especially in the form of ultrashort laser pulses.[3–7] Hence, gold nanoparticles illuminated at their localized surface plasmon resonance (LSPR) wavelength can generate ROS that may, in a living environment, induce necrosis and apoptosis of cells.[3,4,8–12] Indeed, a nanoplasma can be created through the multiphotonic ejection of electrons from the nanoparticles to the surrounding environment and/or by plasmon-enhanced electromagnetic breakdown, leading to •OH and H_2O_2 production. $^1O_2$ is sensitized by Dexter energy transfer between the "hot" electrons and the dissolved triplet oxygen ($^3O_2$) at the very vicinity of the nanoparticles. O_2^- can also be produced by hot-electron transfer from the nanoparticles to the dissolved oxygen.[6] While these mechanisms make gold nanoparticles efficient for use in PDT, they have to be avoided for other applications in biology and biomedicine where the biological environment of the nanoparticles and/or their biofunctionalization need to be preserved under illumination. For instance, when plasmonic nanoparticles are used for gene therapy, based on siRNA or antisense DNA delivery, it is highly important to prevent the cells from being filled with ROS. Indeed, ROS may interact with DNA in the nucleus, forming adducts, either leading to mutagenesis, or directly being detrimental for cell survival by blocking the progression of DNA/RNA polymerases. Alternatively —and depending on their nature or location—, ROS may also have a direct effect on the integrity of membranes (plasma membrane or inner mitochondrial membrane) causing cell necrosis or apoptosis.

Silica-coated gold nanoparticles hold great promises for a wide range of applications in biomedicine and biology. Thanks to their high thermodynamic and chemical stability, they are used for photoacoustic imaging,[13–15] cell tracking,[16] and photothermal therapy.[17,18] The silica shell prevents gold nanoparticles from shape modification under high light intensity levels[13] and reduces the plasmon resonance coupling between nanoparticles, preserving thus their optical properties.[16] Silica-coated gold nanoparticles are also exploited for drug delivery,[19] biosensing,[20] and dual-mode/multimodal imaging[21] thanks to the porosity of the silica shell. Indeed, the mesoporous silica shell can be loaded with drugs, dyes, or imaging agents through physical adsorption or covalent attachment. In addition, the silica shell makes gold nanorods

[a] Université Paris-Saclay, CNRS, ENS Paris-Saclay, CentraleSupélec, LuMIn, 91190 Gif-sur-Yvette, France
[b] Université Paris-Saclay, CEA, CNRS, NIMBE, 91190 Gif-sur-Yvette, France
[c] Université Paris-Saclay, CNRS, ENS Paris-Saclay, PPSM, 91190 Gif-sur-Yvette, France
* Corresponding author. E-mail address: bruno.palpant@universite-paris-saclay.fr
Electronic Supplementary Information (ESI) available: Additional images of the silica-coated gold nanorods (AuNRs@SiO_2); Method of inserting the solution into the capillary; Additional experimental data; BEM numerical simulations - Extinction cross sections; BEM numerical simulations – Maps of the optical near-field enhancement around the AuNR and AuNR@SiO_2. See DOI: 10.1039/x0xx00000x

(AuNRs) biocompatible by removing the usual highly cytotoxic stabilizing molecules, CTAB (hexadecyltrimethylammonium bromide), from their surface. Further, it has been shown to prevent the formation of a protein corona around the nanoparticles.[22,23] Finally, numerous studies reported in the literature have demonstrated that silica-coated gold nanoparticles are efficiently internalized in different types of cells.[16,22,24–27] It has been shown that the uptake of gold nanoparticles is enhanced by a factor 5 after coating with a silica layer, without abnormal cytotoxicity and proliferation.[14] Some groups even developed strategies based on the engineering of the AuNP surface chemistry to add the selectivity of the uptake process for specific cells.[28–30]

In this article, we demonstrate that the silica shell prevents ROS production by the nanoparticles in addition to the above benefits. This makes silica-coated gold nanoparticles, on the one hand, not suitable for use as direct photosensitizers in PDT, but on the other hand, safe for many other applications in biomedicine and biology.

Materials and methods

Synthesis of gold nanorods and replacement of CTAB by PEG-SH in water

Gold nanorods (AuNRs) are synthetized using a seeded growth method in the presence of the CTAB surfactant, following the method proposed by Murray's group.[31] As-synthesized AuNRs are then centrifuged three times at 9000 g to remove excessive CTAB and chemicals and finally dispersed in an aqueous solution containing 1 mM CTAB for long-term stability. The surfactant exchange, *i.e.*, the replacement of CTAB by HS-PEG (thiolated polyethylene glycol) (5-kDa, from TCI), is performed following the multi-stage protocol developed by Mehtala *et al*.[32] in order to obtain a drastic reduction, down to trace levels, of the number of CTAB molecules bound to the gold surface. In this work, we have used the same protocols (synthesis and surfactant exchange from Refs. 22 and 23) as those detailed in a recent study.[33] The PEG-stabilized AuNRs obtained in this way are used as reference materials for measuring ROS production.

Synthesis of AuNR@SiO_2 nanorods

Many sol-gel methods can be found in the literature for coating gold nanoparticles with a silica shell. Indeed, depending on the surfactant at the surface of the gold nanoparticle, the reaction medium (alkaline alcohol-water mixture or pure water) and the alkoxysilane derivatives used as the silica precursor, various silica thicknesses and porosities can be obtained (see recent reviews[20,34–36]). Here, the coating of CTAB-stabilized AuNRs (AuNR@CTAB) is performed using the 3-mercaptopropyl trimethoxysilane derivative (MPTMS) as the silica precursor and following the recommendations presented in Refs. 37 and 38. The CTAB surfactant acts as a structure-directing agent for the silica shell formation on the surface of AuNRs. Specifically, 10 μL of a 5 vol % MPTMS in ethanol and 50 μL of a 0.1 M aqueous NaOH solution are added successively to 3.8 mL of a AuNRs solution (1 mM CTAB). After the mixture is left to react for 2 hours at 50 °C, the resultant silica-coated gold nanorods, AuNRs@SiO_2, are washed by centrifugation and dispersed in water. Scanning electron microscopy (SEM) and transmission electron microscopy (TEM) are used to visualize the NPs at different scales.

Sample preparation

The samples are prepared by sucking into a square borosilicate capillary (CM Scientific, Product n◦ 8100-100, length 100 mm, Square ID: 1.00 x 1.00 mm², wall thickness 0.2 mm)[39] a solution containing AuNRs (respectively AuNRs@SiO_2) and a fluorescent probe specific to the ROS tracked. The capillary is then sealed with two putty plugs to limit the gas exchanges between the external environment and the solution. The method for introducing the solution into the capillary is described in detail in the electronic supplementary information (ESI).

The fluorescent reagents used to detect specific ROS are Singlet Oxygen Sensor Green (SOSG) and Dihydrorhodamine 123 (DHR). The SOSG probe is highly sensitive to singlet oxygen ($^1O_2$).[40] The DHR reagent detects both $^1O_2$[41] and hydroxyl radical (•OH)[42] while being insensitive to superoxide (O_2^-) and hydrogen peroxide (H_2O_2) in the absence of ROS interconverting substrates.[42–44] The SOSG and DHR probes turn from dark to fluorescent molecules upon oxidation by ROS. SOSG and DHR are provided in vials containing receptively 100 µg and 2 mg of solid product.[45,46] The aqueous SOSG is prepared by dissolving 100 µg of solid SOSG in 33 µL of methanol.[47] The solutions used for the experiments with AuNRs and AuNRs@SiO_2 are obtained by adding 4 µL of aqueous SOSG to 2 mL of AuNRs stabilized by HS-PEG ligand in water (respectively AuNRs@SiO_2 in water). The concentrations of AuNRs and of AuNRs@SiO_2 correspond to an optical density of ~1 at 1030 nm wavelength through a 1-cm optical path length. The final SOSG concentration is 10 µM. We use PEG rather than CTAB as a nanoparticle stabilizer because CTAB alters the emission properties of SOSG and its response to $^1O_2$, as recently demonstrated.[33] Concerning DHR, 2 mg of the solid product are dissolved in 2 mL of dimethyl sulfoxide (DMSO). The solutions for the experiments are prepared by mixing 1 mL of PEGylated AuNRs in water (respectively AuNRs@SiO_2 in water) with 10 µL of aqueous DHR.[48] The concentration of DHR in the final solutions is 28.9 µM.

Experiment

Fluorescence measurements are carried out using the experimental setup previously described,[33] the working principle of which is recalled in Fig. 1. The sample is positioned at the objective focal plane (CFI Plan Apo DM Lambda 60XC, N.A. 0.94) of an epifluorescence microscope (TE2000-U, Nikon) and illuminated in widefield mode. The longitudinal LSPR of the AuNRs (respectively AuNRs@SiO_2) is excited at 1030 nm wavelength (1.2 eV photon energy) using the pulsed output of a femtosecond Yb:KGW laser (t-pulse 200, Amplitude Systèmes, repetition rate 10 MHz, pulse width 400 fs). The polarization of the laser beam is circular in order to excite the randomly-oriented nanoparticles. A laser beam at 515 nm wavelength (2.4 eV) is also generated by focalizing the 1030-nm beam into a

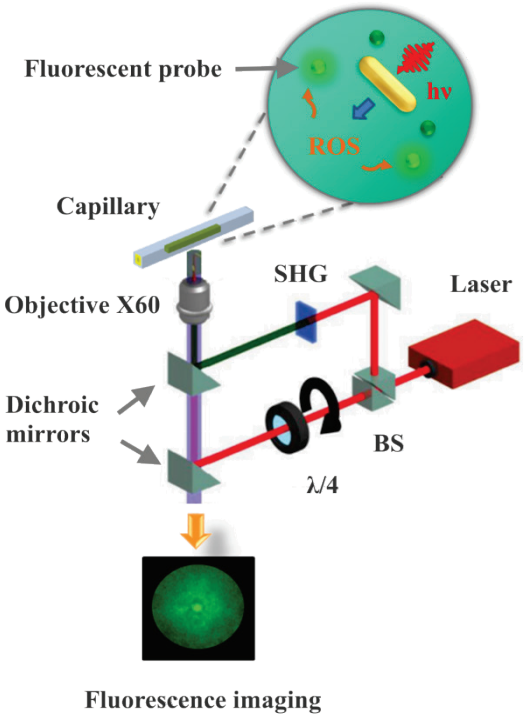

Fig. 1. Schematic representation of the experimental setup. SHG: Second Harmonic Generation, BS: Beam Splitter. Emission dichroic mirrors bandwidth: 523-780 nm.

nonlinear crystal of β-BaB_2O_4. The 515-nm laser beam is used to excite the SOSG and the DHR fluorescent probes. The diameters of illumination profiles at the sample plane are 25 µm@1/e² and 45 µm@1/e² for 1030 nm and 515 nm, respectively. The peak intensity at the sample surface for the 515 nm laser beam is about 1.35 MW cm^{-2}, and that of the 1030 nm beam is adjusted from 152 to 640 MW cm^{-2}. Real-time visualization of the sample fluorescence is achieved by sending the collected light to a CCD camera (Retiga R1, QImaging).

Simulation of the optical properties

Numerical calculations of the extinction cross-section and the optical near-field enhancement are carried out by the boundary element method (BEM)[49] using the MNPBEM17 toolbox.[50,51] As the nanorod dimensions are not negligible against the laser wavelength, the retarded wave effect is considered. The simulations are conducted for individual AuNR and AuNR@SiO_2 nanoparticles. In order to simulate the optical properties of the most-responding nanoparticles, we have chosen a combination of aspect ratio (AR = length/diameter) and silica thickness within the distributions observed in TEM to make the calculated resonance match the experimental laser wavelength (see the electronic supplementary information file). The stationary dielectric function of gold is taken from Johnson and Christy.[52] Its pulse-induced ultrafast evolution is then calculated based on the model previously developed in our group, accounting for the athermal regime for the electron distribution.[53] At each time step, the instantaneous power absorbed from the pulse is determined from the absorption cross-section given by the BEM calculation of the nanoparticle properties at the preceding step. The AuNR and AuNR@SiO_2 in water are irradiated at λ=1030 nm by a 400-fs laser pulse with a peak intensity I_0 = 152 MW cm^{-2}. These parameters correspond to those used in the experimental investigation. Once the transient dielectric function of the metal is determined with a 1-fs time pitch, the subsequent dynamical evolution of the optical near-field along the pulse passage is computed by the BEM every 100 fs. In order to efficiently characterize the influence of different parameters (position in space, thickness of the silica layer), we define the effective optical near-field enhancement, similarly as was done previously for the effective absorption cross-section,[54] as the average value of the field enhancement factor (ratio of the amplitudes of the local plasmonic field, E_p, and the incident field, E_0) weighted by the instantaneous value of the laser intensity:

$$\left|E_p/E_0\right|_{eff} = \frac{\int \left|E_p/E_0\right|(t)\, I(t)\, dt}{\int I(t) dt} \qquad (1)$$

where $I(t)$ is the instantaneous laser intensity. The near-field enhancement is then monitored at its maximum value in space, *i.e.*, at the nanorod tip, where the plasmonic field amplification may induce the highest effects on the ROS production.

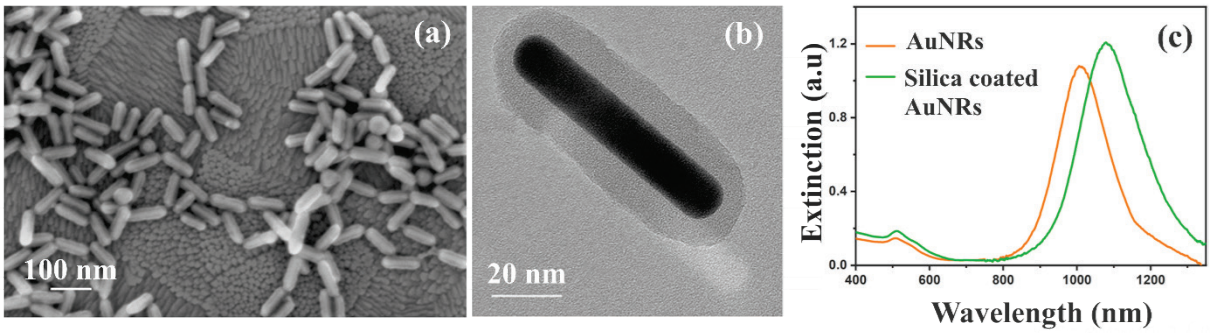

Fig.2. (a) SEM image and (b) TEM image of AuNRs@SiO_2 12.2 ± 1.3 nm thick and 73.0 ± 8.3 nm long. The average thickness of the silica coating is 8.7 ± 1.3 nm. (c) Optical extinction spectra of AuNRs stabilized by HS-PEG ligand in water (orange curve) and of AuNRs@SiO_2 in water (green curve) with longitudinal LSPR peaks observed at 1013 nm and 1082 nm, respectively.

Results and discussion

SEM and TEM images [Figs. 2(a) and 2(b)] show a rather homogeneous silica coating of 8.7 ± 1.3 nm average thickness. Let us first underline that a too thin silica coating (<3-4 nm) would not be suitable because a certain percentage of rods would exhibit bare tips (without silica), due to the fact that the coating is not perfectly homogeneous all around the gold [thinner at the ends, see Fig. 2(b)]. Contrary to the coating procedures leading to mesoporous silica, in the present study, the silanisation reaction leads to a dense silica coating with small pores impeding on purpose the effective diffusion of molecules across the shell [see TEM images on Figs. 2(b) and S1].[37] This silica coating induces a redshift (~65 nm) of the LSPR compared with PEGylated AuNRs and increases the molar extinction coefficient, as displayed in Fig. 2(c), due to the higher refractive index of amorphous silica (1.46) than that of water. The silica layer is chosen thin enough so that the spectral redshift of the longitudinal LSPR still enables a strong absorption at the excitation wavelength (1030 nm).

The SOSG and DHR emission intensities are recorded in the presence of PEGylated AuNRs, and compared under identical conditions with AuNRs@SiO_2, acting as ROS photosensitizers. The results obtained are depicted in Figs. 3 and 4, respectively. The samples are first illuminated for 10 s with a laser beam at 515 nm wavelength to record the initial emission of the two probes. A laser beam at 1030 nm is added for 10 s to excite the longitudinal LSPR of nanoparticles and generate ROS. The wavelength of the IR laser beam is close to the longitudinal LSPR peaks of the PEGylated AuNRs and AuNRs@SiO_2, which are registered at 1013 nm and 1082 nm, respectively [Fig. 2(c)]. The emission intensity is collected for IR power densities ranging from 152 MW cm^{-2} to 641 MW cm^{-2}. At last, the IR laser is turned

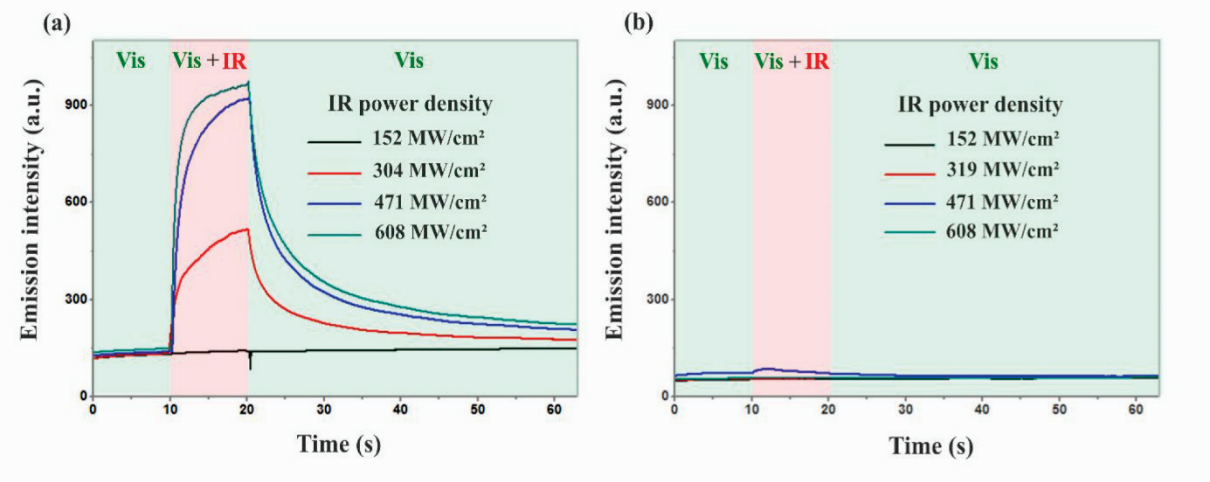

Fig. 3. SOSG emission intensity in the presence of (a) PEGylated AuNRs and (b) AuNRs@SiO_2 acting as ROS photosensitizers, in water. The SOSG reagent detects $^1O_2$. The SOSG fluorescence is recorded before, during and after the excitation of the longitudinal LSPR of the nanoparticles (λ = 1030 nm, IR) with pulse peak intensities ranging from 152 to 608 MW cm^{-2}. The SOSG probe is excited at 515 nm wavelength (Vis). The peak intensity for the 515 nm laser pulses is 1.35 MW cm^{-2}.

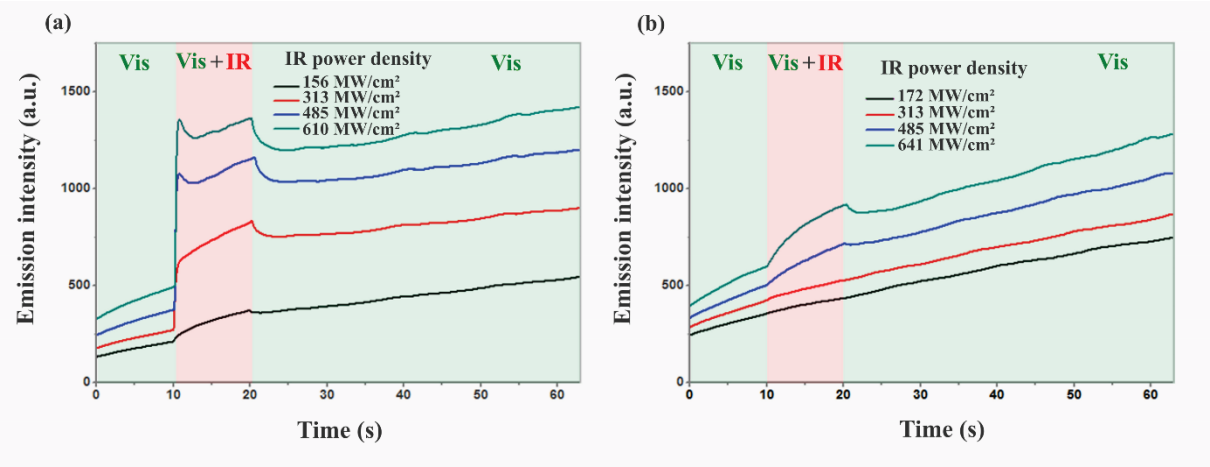

Fig. 4. DHR emission intensity in the presence of (a) PEGylated AuNRs and (b) AuNRs@SiO_2 acting as ROS photosensitizers, in water. The DHR reagent detects $^1O_2$ and •OH. The DHR fluorescence is recorded before, during and after the excitation of the longitudinal LSPR of the nanoparticles (λ = 1030 nm, IR) with pulse peak intensities ranging from 156 to 641 MW cm^{-2}. The DHR probe is excited at 515 nm wavelength (Vis). The peak intensity for the 515 nm laser pulses is 1.35 MW cm^{-2}.

off, leaving only the 515 nm one, to record the fluorescence of SOSG and DHR after the excitation of the surface plasmons.

An initial SOSG fluorescence [Figs. 3(a) and 3(b)] is observed before the excitation of the PEGylated AuNRs and AuNRs@SiO_2. This initial emission is due to the presence of oxidized SOSG molecules,[33] which most probably stems from the synthesis of $^1O_2$ by SOSG itself upon the irradiation at 515 nm wavelength.[55] In the case of DHR [Figs. 4(a) and 4(b)], the constant increase of the fluorescence background at 515 nm before the excitation of the nanoparticle LSPR results from the oxidation of DHR by the laser and dioxygen.[48] The SOSG and DHR fluorescence increase is observed while exciting the PEGylated AuNRs with the laser beam at 1030 nm wavelength, indicating the generation of $^1O_2$ and •OH by the PEGylated AuNRs. In contrast, the rise of both the SOSG and DHR emissions is negligible for AuNRs@SiO_2, indicating that the silica shell prevents $^1O_2$ and •OH production under IR excitation. After turning off the irradiation at 1030 nm, the SOSG emission intensity decreases and returns gradually back to its initial value due to the diffusion of the oxidized SOSG molecules outside the field of view and/or the reversibility of the anthracene peroxidation.[56] The DHR emission also decreases following the diffusion of the DHR molecules oxidized by ROS, but the oxidation of unreacted DHR molecules by the 515-nm laser and dioxygen quickly offsets this decrease. Additional data are provided in the ESI to ensure the reproducibility of the results.

$^1O_2$ is produced by Dexter energy transfer[57] between the dissolved triplet oxygen ($^3O_2$) and the hot electrons generated by the plasmon excitation.[6,11] This process requires significant overlap of the relevant electronic wave functions; as a result, the electron exchange can only occur at short distances, typically within 1 nm. Since the thickness of the silica coating is 8.7 ± 1.3 nm, the Dexter electron exchange between the nanoparticle and the dissolved $^3O_2$ cannot occur, and $^1O_2$ is not produced. In addition, the longitudinal LSPR wavelengths of the PEGylated AuNRs and AuNRs@SiO_2 are outside the $^3O_2 \rightarrow {}^1O_2$ absorption band (1270 nm); a direct excitation of $^1O_2$ by the plasmon field is then not expected.[58] All of this explains the negligible increase of SOSG emission during the excitation of the AuNRs@SiO_2 longitudinal LSPR. In contrast, the authors of Ref. 59 reported enhanced production of $^1O_2$ *in cellulo* under plasmonic excitation of gold nanospheres after coating with a silica layer, which was attributed to the much weaker aggregation of the coated nanoparticles than that of bare gold nanospheres. However, in these irradiation experiments, lasting for 3 to 16 hours, the porosity of the 5-nm silica layer (possibly enabling the insertion of the liquid medium in close contact with gold) was not assessed.

Let us now discuss the case of hydroxyl radical. The generation of •OH is induced by the breaking down of water molecules by electron emission from the nanoparticles and/or by direct plasmon-enhanced electromagnetic breakdown.[6] In the one hand, in the case of AuNRs@SiO_2, the electron ejection from the nanoparticles to the surrounding environment is blocked by the silica shell. Such a blocking was already demonstrated and used in other contexts, where the emission of hot charge carriers from plasmonic nano-objects needs to be inhibited.[60–62] Besides, when irradiated by X-rays, high-*Z* nanoparticles in water can emit electrons by different mechanisms; this phenomenon is used in sensitisation (aka enhancement) of radiotherapy. In this context, it was shown that coating nanoparticles with a silica layer blocks the short-traveling low-energy electron emission, while high-energy electrons, traveling for microns, can still be emitted.[63] These examples all support the hindering of electron ejection from our AuNR@SiO_2 nano-objects due to the silica shell, as the multiphotonic processes in metal provide electrons with a few eV kinetic energy only.[53]

On the other hand, BEM-based numerical simulations of the optical near-field around the AuNRs and AuNRs@SiO_2 are also conducted to evaluate the effect of the silica shell on the optical field enhancement resulting from the plasmon excitation. The simulations are carried out for a single AuNR and a single AuNR@SiO_2 as described in the Materials and Methods section. The calculated extinction cross-sections are given in the ESI and show a longitudinal LSPR at 1014 nm and 1030 nm, respectively. The dynamics of the field enhancement factor throughout the laser pulse passage and the maps of the optical near-field enhancement around the nanoparticles are displayed in Fig. 5. First, it can be seen in Fig. 5(a) that the instantaneous field enhancement factor decreases with time for both nanoparticles. This is due to the progressive quenching of the absorption cross-section upon further energy input from the light pulse, as demonstrated earlier.[54] Besides, the results show a decrease in the optical near-field enhancement after adding the silica shell. The effective field enhancement factor at the tip of the rod [red arrow on Fig. 5(b)] (see the Materials and Methods section) for the AuNR@SiO_2 is worth 5.9, which is six times weaker than the value obtained for the AuNR (35.1). As a result, the probability of inducing the plasmon-enhanced electromagnetic breakdown of water decreases. In addition to the electron emission blockage, this explains the significant decrease in the •OH production after coating AuNRs with silica. Let us notice that the efficiency of such a coating for reducing the production of free radicals was already demonstrated *in cellulo*.[22] The authors interpreted this result as due to the absence of a protein corona around the AuNRs@SiO_2, contrary to the case of bare AuNRs. We demonstrate here that invoking the protein corona is not necessary to explain the inhibition of ROS generation from AuNRs@SiO_2 under laser light irradiation.

These findings are further reinforced by the equivalent set of results obtained with AuNRs coated with a 5.0-nm SiO_2 layer, presented in the ESI file (§ III and IV). The production of ROS is hindered by at least one order of magnitude when coating bare AuNRs with a 5.0- or 8.7-nm silica layer, whatever the laser power within our range of investigation. Furthermore, the thicker the silica shell, the better the inhibition of ROS generation (see ESI, § IV). The potential barrier for the possibly photo-emitted electrons to be extracted out of the nanoparticles is slightly lower for the thinner silica shell. In addition, the near-field enhancement at the nanoparticle tips is larger for the thinner silica shell than for the thicker one, as

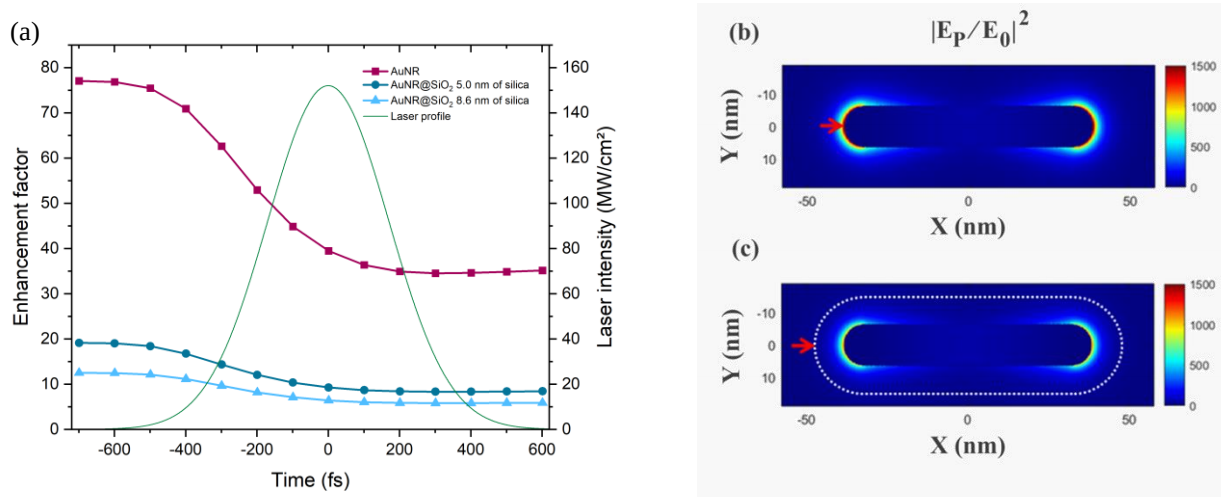

Fig.5. BEM numerical simulations for different nanoparticles in water. (a) Dynamics of the field enhancement factor $|E_p/E_0|$ at the nanoparticle tip (left scale) along the laser pulse passage (right scale) for a AuNR, a AuNR@SiO_2 with 5.0-nm thick silica shell, and a AuNR@SiO_2 with 8.6-nm thick silica shell. E_p and E_0 are respectively the local plasmonic field and the incident electric field. The field enhancement factors are monitored at the tip of the nanorods [red arrows in (b) and (c)]. (b) Color-scale map of the optical near-field intensity enhancement around the AuNR and (c) AuNR@SiO_2 with 8.6-nm thick silica shell. The maps are collected at the maximum of the laser pulse (time = 0 fs). The AuNR and AuNR@SiO_2 are excited at λ=1030 nm (IR) with longitudinal polarization. The dashed white contour represents the outer surface of the SiO_2 layer.

shown by the BEM calculation reported in Fig. 5(a). However, the field enhancement in the two cases remains far weaker than that in the case of the bare AuNRs. This explains that the optical breakdown of water and dioxygen molecules in the enhanced plasmonic near-field is much less probable with these silica coatings.

Conclusions

We have shown through fluorescence imaging that a dense silica shell with small pores prevents the generation of $^1O_2$ and •OH by gold nanoparticles under irradiation at their plasmon resonance. Indeed, the silica layer separates the dissolved $^3O_2$ from the nanoparticle surface, hindering thus the production of $^1O_2$ by Dexter energy transfer between the $^3O_2$ and the hot electrons generated by the plasmon excitation. In addition, it has been shown through BEM numerical simulations that the silica shell lessens the optical field enhancement resulting from the plasmon excitation. As the silica shell also prevents electron emission, the two possible ways of production of •OH are blocked. Consequently, silica-coated gold nanoparticles are not suitable for use as direct photosensitizers in PDT but are safer than pure gold nanorods for a range of other applications in biology and biomedicine.

Author Contributions

S. Mitiche: Conceptualization, Investigation, Validation, Writing – original draft, Visualization, Writing – review & editing.

S. Gueffrache: Conceptualization, Numerical simulations, Writing – original draft.

S. Marguet: Conceptualization, Resources, Funding acquisition, Writing – original draft, Writing – review & editing.

J.-F. Audibert: Conceptualization, Resources, Writing - review & editing.

R. B. Pansu: Conceptualization, Resources, Funding acquisition, Writing – review & editing.

B. Palpant: Conceptualization, Writing – original draft, Writing – review & editing, Funding acquisition, Supervision, Project administration.

Conflicts of interest

There are no conflicts to declare.

Acknowledgements

The authors are grateful to the financial support received from the “Plan Cancer” managed by the French ITMO Cancer (n◦17CP077–00, project HEPPROS). This research is also supported by a public grant overseen by the French National Research Agency (ANR) as part of the “Investissements d’Avenir” program (reference: ANR-10-LABX-0035, Labex NanoSaclay). The authors thank M. Vallet for the TEM imaging.

Notes and references

1 A. Quintanilha, *Reactive Oxygen Species in Chemistry, Biology, and Medicine*, Springer, Boston, MA, 1988.

2 G. Buonocore, S. Perrone and M. L. Tataranno, Oxygen toxicity: chemistry and biology of reactive oxygen species, *Semin. Fetal Neonatal Med.*, 2010, **15**, 186–190.

3 R. Vankayala, Y.-K. Huang, P. Kalluru, C.-S. Chiang, and K. C. Hwang, First demonstration of gold nanorods-mediated photodynamic therapeutic destruction of tumors via near infrared light activation, *Small*, 2014, **10**, 1612–1622.

4 T. Labouret, J. F. Audibert, R. B. Pansu and B. Palpant, Plasmon-assisted production of reactive oxygen species by single gold nanorods, *Small*, 2015, **11**, 4475–4479.

5 See for instance: J. Kuncewicz J. M. Dąbrowski, A. Kyzioł, M. Brindell, P. Łabuz, O. Mazuryk, W. Macyk, and G. Stochel, Perspectives of molecular and nanostructured systems with *d*- and *f*-block metals in photogeneration of reactive oxygen species for medical strategies, *Coord. Chem. Rev*., 2019, **398**, 113012.

6 E. Carrasco, J. C. Stockert, Á. Juarranz and A. Blázquez-Castro, Plasmonic hot-electron reactive oxygen species generation: fundamentals for redox biology, *Front. Chem.*, 2020, **8**, 1160.

7 M. R. Younis, G. He, J. Qu, J. Lin, P. Huang, and X.-H. Xia, Inorganic nanomaterials with intrinsic singlet oxygen generation for photodynamic therapy, *Adv. Sci.*, 2021, **8**, 2102587.

8 L. Minai, D. Yeheskely-Hayon, and D. Yelin, High levels of reactive oxygen species in gold nanoparticle-targeted cancer cells following femtosecond pulse irradiation, *Sci. Rep.*, 2013, **3**, 2146.

9 L. Gao, R. Liu, F. Gao, Y. Wang, X. Jiang and X. Gao, Plasmon-mediated generation of reactive oxygen species from near-infrared light excited gold nanocages for photodynamic therapy in vitro, *ACS Nano*, 2014, **8**, 7260–7271.

10 L. Minai, A. Zeidan, D. Yeheskely-Hayon, S. Yudovich, I. Kviatkovsky, and D. Yelin, Experimental proof for the role of nonlinear photoionization in plasmonic phototherapy, *Nano Lett.*, 2016, **16** (7), 4601–4607.

11 S. J. Chadwick, D. Salah, P. M. Livesey, M. Brust and M. Volk, Singlet oxygen generation by laser irradiation of gold nanoparticles, *J. Phys. Chem. C*, 2016, **120**, 10647–10657.

12 Y. Feng, Y. Chang, X. Sun, Y. Cheng, R. Zheng, X. Wu, L. Wang, X. Ma, X. Li and H. Zhang, Differential photothermal and photodynamic performance behaviors of gold nanorods, nanoshells and nanocages under identical energy conditions, *Biomater. Sci.*, 2019, **7**, 1448–1462.

13 Y.-S. Chen, W. Frey, S. Kim, K. Homan, P. Kruizinga, K. Sokolov and S. Emelianov, Enhanced thermal stability of silica-coated gold nanorods for photoacoustic imaging and image-guided therapy, *Opt. Express*, 2010, **18**, 8867.

14 J. V. Jokerst, M. Thangaraj, P. J. Kempen, R. Sinclair and S. S. Gambhir, Photoacoustic imaging of mesenchymal stem cells in living mice via silica-coated gold nanorods, *ACS Nano*, 2012, **6**, 5920–5930.

15 G. P. Luke, A. Bashyam, K. A. Homan, S. Makhija, Y. S. Chen and S. Y. Emelianov, Silica-coated gold nanoplates as stable photoacoustic contrast agents for sentinel lymph node imaging, *Nanotechnology*, 2013, **24**, 455101.

16 P. P. Joshi, S. J. Yoon, Y.-S. Chen, S. Emelianov and K. V. Sokolov, Development and optimization of near-IR contrast agents for immune cell tracking, *Biomed. Opt. Express*, 2013, **4**, 2609.

17 S. Kim, Y. S. Chen, G. Luke and S. Emelianov, In-vivo ultrasound and photoacoustic image-guided photothermal cancer therapy using silica-coated gold nanorods, *IEEE Trans. Ultrason. Ferroelectr. Freq. Control*, 2014, **61**, 891–897.

18 V. T. T. Duong, A. D. Phan, N. T. H. Lien, D. T. Hue, D. Q. Hoa, D. T. Nga, T. H. Nhung and N. A. Viet, Near-infrared photothermal response of plasmonic gold-coated nanoparticles in tissues, *Phys. status solidi A*, 2018, **215**, 1700564.

19 A. S. Monem, N. Elbialy and N. Mohamed, Mesoporous silica coated gold nanorods loaded doxorubicin for combined chemo–photothermal therapy, *Int. J. Pharm.*, 2014, **470**, 1–7.

20 V. Pellas, D. Hu, Y. Mazouzi, Y. Mimoun, J. Blanchard, C. Guibert, M. Salmain, and S. Boujday, Gold nanorods for LSPR biosensing: Synthesis, coating by silica, and bioanalytical applications, *Biosensors*, 2020, **10**, 146.

21 Y. Zhao, F. Ye, T. B. Brismar, X. Li, R. He, R. Heuchel, R. El-Sayed, N. Feliu, W. Zheng, S. Oerther, J. Dutta, W. J. Parak, M. Muhammed and M. Hassan, Multimodal imaging of pancreatic ductal adenocarcinoma using multifunctional nanoparticles as contrast agents, *ACS Appl. Mater. Interfaces*, 2020, **12**, 53665–53681.

22 M. Das, D. K. Yi, S. S. A. An, Analyses of protein corona on bare and silica-coated gold nanorods against four mammalian cells, *Int J Nanomedicine*, 2015, **10** (1), 1521–1545.

23 J. Mosquera, I. García, M. Henriksen-Lacey, G. González-Rubio, and L. M. Liz-Marzán, Reducing protein corona formation and enhancing colloidal stability of gold nanoparticles by capping with silica monolayers, *Chem. Mater*, 2019, **31** (1), 57–61.

24 X. Sun, Y. Jin, H. Wang, N. Feng, Z. Li, D. Liu, K. Ge, H. Liu, J. Zhang, and X. Yang, A NIR-light activated nanoplatform for sensitizing triple negative breast cancer against therapeutic resistance to enhance the treatment effect, *J. Mater. Chem. B*, 2018, **6**, 6950.

25 Z. Zhang, L. Wang, J. Wang, X. Jiang, X. Li, Z. Hu, Y. Ji, X. Wu, and C. Chen, Mesoporous silica-coated gold nanorods as a light-mediated multifunctional theranostic platform for cancer treatment, *Adv. Mater.*, 2012, **24**, 1418.

26 J. Wang, W. Zhang, S. Li, D. Miao, G. Qian, and G. Su, Engineering of porous silica coated gold nanorods by surface-protected etching and their applications in drug loading and combined cancer therapy, *Langmuir*, 2019, **35**, 14238.

27 H. Guo, Shen Yi, K. Feng, Y. Xia, X. Qua, F. Wan, L. Chen, and C. Zhang, In situ formation of metal organic framework onto gold nanorods/mesoporous silica with functional integration for targeted theranostics, *Chem. Engineer. J*., 2021, **403**, 126432.

28 J. Liu, C. Detrembleur, M. C. De Pauw-Gillet, S. Mornet, C. Jérôme, and E. Duguet, Gold nanorods coated with mesoporous silica shell as drug delivery system for remote near infrared light-activated release and potential phototherapy, *Small*, 2015, **11**, 2323.

29 Y. Wang, L. Wang, L. Guo, M. Yan, L. Feng, S. Dong, and J. Hao, Photo-responsive magnetic mesoporous silica nanocomposites for magnetic targeted cancer therapy, *New J. Chem*., 2019, **43**, 4908.

30 C. Li, K. Feng, N. Xie, W. Zhao, L. Ye, B. Chen, C.-H. Tung, and L.-Z. Wu, Mesoporous silica-coated gold nanorods with designable anchor peptides for chemo-photothermal cancer therapy, *ACS Appl. Nano Mater*., 2020, **3**, 5070.

31 X. Ye, C. Zheng, J. Chen, Y. Gao, and C.B. Murray, Using binary surfactant mixtures to simultaneously improve the dimensional tunability and monodispersity in the seeded growth of gold nanorods, *Nano Lett.*, 2013, **13**, 765–771.

32 J. G. Mehtala, D. Y. Zemlyanov, J. P. Max, N. Kadasala, S. Zhao, and A. Wei, Citrate-stabilized gold nanorods, *Langmuir*, 2014, **30**, 13727–13730.

33 S. Mitiche, J.-F. Audibert, S. Marguet, B. Palpant, and R. B. Pansu, The effect of gold nanoparticle capping agents on $^1O_2$ detection by singlet oxygen sensor green, *J. Photochem. Photobiol. A Chem.*, 2021, **410**, 113170.

34 N. D. Burrows, W. Lin, J. G. Hinman, J. M. Dennison, A. M. Vartanian, N. S. Abadeer, E. M. Grzincic, L. M. Jacob, J. Li and C. J. Murphy, Surface chemistry of gold nanorods, *Langmuir*, 2016, **32**, 9905–9921.

35 C. Hanske, M. N. Sanz-Ortiz and L. M. Liz-Marzán, Silica-coated plasmonic metal nanoparticles in action, *Adv. Mater.*, 2018, **30**, 1707003.

36 A. F. Moreira, C. F. Rodrigues, C. A. Reis, E. C. Costa and I. J. Correia, Gold-core silica shell nanoparticles application in imaging and therapy: A review, *Microporous Mesoporous Mater.*, 2018, **270**, 168–179.

37 N. Liu, B. S. Prall, and V. I. Klimov, Hybrid gold/silica/nanocrystal-quantum-dot superstructures: synthesis and analysis of semiconductor−metal interactions, *J. Am. Chem. Soc.*, 2006, **128**, 15362–15363.

38 K. W. Shah, T. Sreethawong, S.-H. Liu, S.-Y. Zhang, L. S. Tan, and M.-Y. Han, Aqueous route to facile, efficient and functional silica coating of metal nanoparticles at room temperature, *Nanoscale*, 2014, **6**, 11273-11281.

39 Hollow Square Capillaries, https://www.cmscientific.eu/proddetail.php?prod=Hollow+Square+Capillaries+ID+1.00+x+1.00mm+%2822+capillaries+per+pack%29 (accessed 30 August 2021).

40 C. Flors, M. J. Fryer, J. Waring, B. Reeder, U. Bechtold, P. M. Mullineaux, S. Nonell, M. T. Wilson and N. R. Baker, Imaging the production of singlet oxygen in vivo using a new fluorescent sensor, Singlet Oxygen Sensor Green®, *J. Exp. Bot.*, 2006, **57**, 1725–1734

41 D. Costa, E. Fernandes, J. L. M. Santos, D. C. G. A. Pinto, A. M. S. Silva and J. L. F. C. Lima, New noncellular fluorescence microplate screening assay for scavenging activity against singlet oxygen, *Anal. Bioanal. Chem.,* 2007, **387**, 2071–2081.

42 M. Wrona, K. Patel and P. Wardman, Reactivity of 2′,7′-dichlorodihydrofluorescein and dihydrorhodamine 123 and their oxidized forms toward carbonate, nitrogen dioxide, and hydroxyl radicals, *Free Radic. Biol. Med.*, 2005, **38**, 262–270.

43 J. P. Crow, Dichlorodihydrofluorescein and Dihydrorhodamine 123 Are Sensitive Indicators of Peroxynitritein Vitro:Implications for Intracellular Measurement of Reactive Nitrogen and Oxygen Species, *Nitric Oxide*, 1997, **1**, 145–157.

44 J. A. Royall and H. Ischiropoulos, Evaluation of 2′,7′-dichlorofluorescin and dihydrorhodamine 123 as fluorescent probes for intracellular H_2O_2 in cultured endothelial cells, *Arch. Biochem. Biophys.*, 1993, **302**, 348–355.

45 Singlet Oxygen Sensor Green, https://www.thermofisher.com/order/catalog/product/S36002#/S36002, (accessed 30 August 2021).

46 Dihydrorhodamine 123, https://www.sigmaaldrich.com/FR/fr/product/sial/d1054, (accessed 30 August 2021).

47 Singlet Oxygen Sensor Green Reagent, https://www.thermofisher.com/document-connect/document-connect.html?url=https%3A%2F%2Fassets.thermofisher.com%2FTFS-Assets%2FLSG%2Fmanuals%2Fmp36002.pdf&title=U2luZ2xldCBPeHlnZW4gU2Vuc29yIEdyZWVuIFJlYWdlbnQ=, 2004, (accessed 30 August 2021).

48 T. Labouret, Irradiation laser ultrabrève de nanobâtonnets d'or individuels en milieu aqueux : photo-génération de phénomènes d'intérêt biomédical, PhD thesis, Université Paris-Saclay, 2016.

49 F. J. García de Abajo and A. Howie, Retarded field calculation of electron energy loss in inhomogeneous dielectrics, *Phys. Rev. B: Condens. Matter Mater. Phys.*, 2002, **65**, 115418.

50 U. Hohenester and A. Trügler, MNPBEM – A Matlab toolbox for the simulation of plasmonic nanoparticles, *Comput. Phys. Commun.*, 2012, **183**, 370–381.

51 J. Waxenegger, A. Trügler and U. Hohenester, Plasmonics simulations with the MNPBEM toolbox: Consideration of substrates and layer structures, *Comput. Phys. Commun.*, 2015, **193**, 138–150.

52 P. B. Johnson and R. W. Christy, Optical constants of the noble metals, *Phys. Rev. B*, 1972, **6**, 4370–4379.

53 T. Labouret and B. Palpant, Nonthermal model for ultrafast laser-induced plasma generation around a plasmonic nanorod, *Phys. Rev. B*, 2016, **94**, 245426.

54 X. Hou, N. Djellli and B. Palpant, Absorption of ultrashort laser pulses by plasmonic nanoparticles: not necessarily what you might think, *ACS Photonics*, 2018, **5** (9), 3856–3863.

55 X. Ragàs, A. Jiménez-Banzo, D. Sánchez-García, X. Batllori, and S. Nonell, Singlet oxygen photosensitisation by the fluorescent probe Singlet Oxygen Sensor Green®, *Chem. Commun.*, 2009, **20**, 2920–2922.

56 W. Fudickar and T. Linker, Reversible Photooxygenation of alkynylanthracenes: chemical generation of singlet oxygen under very mild conditions, *Chem. – A Eur. J.*, 2011, **17**, 13661–13664.

57 D. L. Dexter, A theory of sensitized luminescence in solids, *J. Chem. Phys.*, 1953, **21**, 836

58 F. Anquez, I. E. Y. Belkoura, P. Suret, S. Randoux, and E. Courtade, Cell death induced by direct laser activation of singlet oxygen at 1270 nm, *Laser Phys.*, 2012, **23**, 025601.

59 K. S. Meena, K. I. Dhanalekshmi, and K. Jayamoorthy, Study of photodynamic activity of Au@SiO_2 core-shell nanoparticles *in vitro*, *Mater. Sci. Eng. C*, 2016, **63**, 317–322.

60 J. Li, S. K. Cushing, F. Meng, T. R. Senty, A. D. Bristow, and N. Wu, Plasmon-induced resonance energy transfer for solar energy conversion, *Nat. Photonics* 2015, **9**, 601.

61 N. Takeyasu, K. Yamaguchi, R. Kagawa, T. Kaneta, F. Benz, M. Fujii, and J. J. Baumberg, Blocking hot electron emission by SiO_2 coating plasmonic nanostructures, *J. Phys. Chem. C*, 2017, **121** (34), 18795–18799.

62 C. Zhan, Z.-Y. Wang, X.-G. Zhang, X.-J. Chen, Y.-F. Huang, S. Hu, J.-F. Li, D.-Y. Wu, M. Moskovits, and Z.-Q. Tian, Interfacial construction of plasmonic nanostructures for the utilization of the plasmon-excited electrons and holes, *J. Am. Chem. Soc.*, 2019, **141** (20), 8053–8057.

63 R. A. Davidson and T. Guo, Average physical enhancement by nanomaterials under X-ray irradiation, *J. Phys. Chem. C*, 2014, **118** (51), 30221–30228.

